Micro-Doppler Shift and Its Estimation in Rotary-Wing UAV Sub-6 GHz Communications

Hsin-An Hou, Li-Chun Wang, *Fellow, IEEE*, and Hsin-Piao Lin, *Member, IEEE*

Abstract— Rotary-wing unmanned aerial vehicles (UAVs) can be potentially used in wireless communications and therefore attract research from both academia and industry recently. However, most UAV air-to-ground channel models under 6 GHz have ignored the micro-Doppler effects due to the UAV's propellers. In this letter, we reveal its principle and develop a method to estimate the micro-Doppler, including sounding waveform design, channel modeling, and Doppler frequency estimation. Our simulation results demonstrate that the estimated root-mean-squared error of micro-Doppler is smaller than 18.83 Hz for 963.09 Hz micro-Doppler frequency shift resulting from the rotation of the propellers in the rotary-wing UAV sub-6 GHz communications systems.

Index Terms—Unmanned aerial vehicles (UAVs), air-to-ground channel, micro-Doppler effects.

I. INTRODUCTION

ROTARY-WING unmanned aerial vehicles (UAVs) play a key role in many commercial applications [1], such as flying camera, package delivery, public safety, and high-precision agriculture. To optimize a UAV communications system, it is critical to understand the air-to-ground channel characteristics. The air-to-ground radio channel of UAV communications has been investigated in [2]–[4], including the large-scale path loss, shadowing, and small-scale multi-path fading. Furthermore, the Doppler effect, caused by the relative movement between the UAV and the ground station, has been investigated in urban, mountain, and desert environments [5], where a measurement platform has been built and an approach to analyze the time and frequency dispersion characteristics has been developed. The short time Fourier transform (STFT) has been used in the above studies.

Hsin-An Hou is with Information and Communications Research Laboratories, Industrial Technology Research Institute, Hsinchu 31040, Taiwan, and also with the Department of Electrical and Computer Engineering, National Yang Ming Chiao Tung University, Hsinchu 300, Taiwan (e-mail: hsinan_hou@itri.org.tw).

Li-Chun Wang is with the Department of Electrical and Computer Engineering, National Yang Ming Chiao Tung University, Hsinchu 300, Taiwan (e-mail: lichun@g2.nctu.edu.tw).

Hsin-Piao Lin is with the Department of Electronics Engineering, National Taipei University of Technology, Taipei 106, Taiwan (e-mail: hplin@ntut.edu.tw).

Complex motions, such as translational and rotational motion, cause the unique frequency modulation of radar signals, called micro-Doppler [6]. The Doppler periodicities and frequencies are proportional to the motor revolution and blade maximum speed as well as those in [7]–[10], respectively. The methods in [7]–[9] extract the spectrogram, cepstrum, and singular vector features from the STFT results of the micro-Doppler signal reflected by an unidentified flying object (UFO) to classify the UFO as a UAV, a bird, or others. Since the micro-Doppler appears in a short duration, i.e., several milliseconds, and also changes continuously over the time [8], [10], the Doppler frequency estimated by STFT adopts longer integration time to increase the frequency resolution resulting in detection failure. Our method conducts the micro-Doppler frequency estimated from the adjacent samples, rather than the analyzed duration of the STFT as [7]–[9], so it can detect the micro-Doppler effect over the sub-6 radio band

To our best knowledge, the micro-Doppler effect for the rotary-wing UAV has been rarely investigated in the existing literature except for our previous work in [10]. Based on a simplified air-to-ground wireless communication model, we have analyzed the micro-Doppler effect caused by propeller's rotation as a function of radio center frequency, motor revolution, propeller's length, and propeller's pitch, where the latter three factors are determined by the UAV's configuration. Since the rotary-wing of a UAV incurs high Doppler frequency on the air-to-ground radio communication, its impact on the performance of UAV communications cannot be ignored. Particularly, systems based on power domain multiplexing technique, such as non-orthogonal multiple access (NOMA), will be significantly affected by the air-to-ground channel dramatically [11], [12].

In this letter, we analyze micro-Doppler shift and develop estimation method for the air-to-ground channel in the sub-6 GHz frequency band, which is the first work in the related topic to the best of our knowledge.

II. MICRO-DOPPLER DOPPLER EFFECT

A. Channel Model

In this section, we will first present the channel model due to micro-Doppler effect, and then present its impact on communication systems. Fig. 1(a) shows a typical quad-copter composed of propellers of one or more blades and driven by independent motors to generate the thrust force to make the UAV take off, land, move, and hover via the mechanical structure. The horizontal reflection expressed by the solid line describes the electromagnetic wave propagation path, which

TABLE I
SYMBOL, PARAMETERS, AND DEFAULT FOR ANALYSIS

Sym.	Parameters	Default
D_p	Diameter of propeller	254 mm
f_m	Motor revolutions	4620 RPM
N_b	Blade number of one propeller	2
f_c	Carrier frequency of the radio	2.5 GHz
d_{UE}	Distance of the UE to the antenna	1000 m
d_{ant}	Distance of the antenna to the propeller axis	200 mm

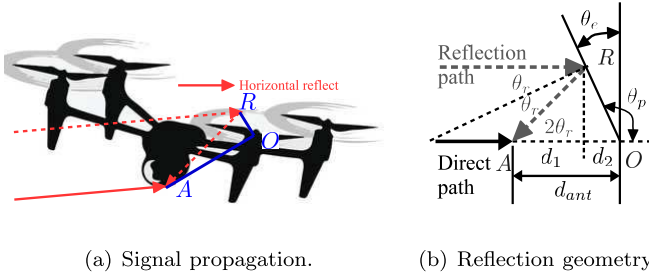(a) Signal propagation.   (b) Reflection geometry.

Fig. 1.   An example of horizontal reflection.

inclines to the reflection point R on the propeller, reflected by the propeller of the rotation center O, then arrives at the antenna A, when the user equipment (UE) is located on a distant range from the UAV in Fig. 1(a). Since the horizontal reflection causes the Doppler effect more seriously than the vertical reflection and vibration [10], we analyze the horizontal reflection channel, with typical technical parameters shown as in Table I.

To find the relationship between the Doppler frequency and the parameters, we extract ΔROA from Fig. 1(a), and illustrate the geometry between propagation path and UAV components in Fig. 1(b), where the propagation path, the propeller, and the antenna are on the same plane. We define a reflection zone angle, θ_{rz}, for which the reflection performs when $|\theta_e(t)| < |\theta_{rz}|$. The phase at time t can be written as

$$\theta_e(t) = 2\pi f_m t + \theta_p(0) + \frac{2m\pi}{N_b} - \frac{\pi}{2}, \tag{1}$$

for $m \in 1, \ldots, N_b$, where $\theta_p(0)$ is the initial angle when $t = 0$; f_m is the revolution of the motor; and N_b is the blade number of the propellers in Table I.

In Fig. 1(b), the reflection inclines to the reflection point R with an angle θ_r. Since the reflection path and the direct path are asymptotically parallel for a long distance between the transmitter and the receiver, and $\angle ROA + \theta_r = \frac{\pi}{2}$, $\theta_e(t) = \theta_r(t)$, $\angle RAO = 2\theta_r(t)$, we can have

$$\begin{cases} d_1 \tan(2\theta_e(t)) = d_2 \tan(\frac{\pi}{2} - \theta_e(t)), \\ d_1 + d_1 = d_{ant}. \end{cases}$$

If $\frac{\theta_e(t) - \pi}{2\pi} \notin \mathbb{Z}$, d_1 and d_2 can be expressed by

$$\begin{aligned} d_1 &= \frac{d_{ant}\left(\tan^4\left(\frac{\theta_e(t)}{2}\right) - 6\tan^2\left(\frac{\theta_e(t)}{2}\right) + 1\right)}{\left(\tan^2\left(\frac{\theta_e(t)}{2}\right) + 1\right)^2} \\ &= d_{ant}(1 - 2\sin^2(\theta_e(t))) = d_{ant}\cos 2\theta_e(t), \end{aligned} \tag{2}$$
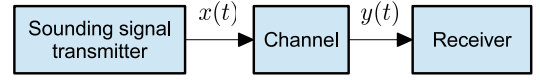

Fig. 2.   Block diagram for the micro-Doppler evaluation.

$$d_2 = \frac{8d_{ant}\tan^2\left(\frac{\theta_e(t)}{2}\right)}{\left(\tan^2\left(\frac{\theta_e(t)}{2}\right) + 1\right)^2} = 2d_{ant}\sin^2(\theta_e(t)). \tag{3}$$

From Fig. 1(b), the relationship between $\theta_e(t)$ and d_2 can be expressed as $d_2 = \overline{OR}\sin\theta_e(t)$. Substituting d_2 and $\overline{OR}$ by $2d_{ant}\sin^2(\theta_e(t))$ and $\frac{D_p}{2}$, respectively. Then, we can obtain $\frac{D_p}{2}\sin\theta_{rz} = 2d_{ant}\sin^2\theta_{rz}$, and

$$\theta_{rz} = \sin^{-1}\left(\frac{D_p}{4d_{ant}}\right). \tag{4}$$

The phase of the traveling wave is the traveling distance, $(1 + \sec 2\theta_e(t))$, divided by wavelength, λ_c. The instantaneous Doppler frequency for the reflection path can be expressed by the differential of the phase of the traveling wave as

$$\begin{aligned} f_{D,r}(t) &= \frac{\mathrm{d}}{\mathrm{d}t}\frac{d_1(1 + \sec 2\theta_e(t))}{\lambda_c} \\ &= \frac{\mathrm{d}}{\mathrm{d}t}\frac{d_{ant}\cos 2\theta_e(t)(1 + \sec 2\theta_e(t))}{\lambda_c} \\ &= \frac{d_{ant}}{\lambda_c}\frac{\mathrm{d}}{\mathrm{d}t}\cos 2\theta_e(t) \\ &= -\frac{4\pi f_m d_{ant} f_c \sin 2\theta_e(t)}{c}. \end{aligned} \tag{5}$$

B. System Model

Fig. 2 shows the system model for the micro-Doppler estimation, which comprises sounding signal transmitter, channel, and receiver. The sounding signal transmitter generates a continuous predetermined sounding waveform $x(t)$ and sends to the receiver to estimate the micro-Doppler effect of the channel from the ground to the UAV. The sounding waveform, $x(t)$, needs to be carefully designed to possess the required time-frequency domain resolution features for measuring the micro-Doppler effect.

According to [10], the air-to-ground channel for the UAV of propellers with one or two blades are usually with two paths: a direct path and a reflection path. The received signal $y(t)$ at the UAV can be expressed as

$$\begin{aligned} y(t) &= a_d(t)x(t - t_d)e^{j\theta_d(t)} \\ &\quad + a_r(t)x(t - t_r)e^{j\theta_r(t)} + w(t), \end{aligned} \tag{6}$$

$$t_d = \frac{d_d(t)}{c}, t_r = \frac{d_r(t)}{c}; \theta_d = \frac{d_d(t)}{\lambda_c}, \theta_r = \frac{d_r(t)}{\lambda_c},$$

where $\{a_d(t), t_d(t), \theta_d(t), d_d(t)\}$ and $\{a_r(t), t_r(t), \theta_r(t), d_r(t)\}$ are the amplitude attenuation factors, propagation delays, phases, and traveling distances of the direct path and the reflection path, respectively; c is the light speed in vacuum; $w(t)$ is additive white Gaussian noise; and $\lambda_c = \frac{c}{f_c}$ is the wavelength of the carrier frequency f_c.

Usually $\Delta t = t_r - t_d$ is very small and can be ignored, but the phase difference $\Delta\theta_r(t) = \theta_d(t) - \theta_r(t)$ cannot be

ignored. Then the received signal can be written as

$$
\begin{aligned}
y(t) = {}& a_d(t)x(t - t_d)e^{j\theta_d(t)} \\
& + a_r(t)x(t - t_d)e^{j(\theta_d(t)+\Delta\theta_r(t))} + w(t).
\end{aligned}
$$

The corresponding discrete–time expression $y(t)$ with a sampling frequency f_s becomes

$$
\begin{aligned}
y[n] = {}& a_d[n]x[n - n_d]e^{j\theta_d[n]} \\
& + a_r[n]x[n - n_d]e^{j(\theta_d[n]+\Delta\theta_r[n])} + w[n], \quad (7)
\end{aligned}
$$

where $y[n] = y(\frac{n}{f_s})$, $x[n] = x(\frac{n}{f_s})$, $a_d[n] = a_d(\frac{n}{f_s})$, $a_r[n] = a_r(\frac{n}{f_s})$, $\theta_d[n] = \theta_d(\frac{n}{f_s})$, $w[n] = w(\frac{n}{f_s})$ and $n_d = \lfloor f_s t_d \rfloor$. When $x[n]$ is normalized by the average power to unit, and the power of the direct path is $\mathrm{E}(|a_d[n]|^2) = \sigma_s^2$, and the power of the reflection path will be

$$
\mathrm{E}(|a_r[n]|^2) = \frac{\sigma_s^2}{10^{\frac{RL+\delta[n]}{10}}}, \quad (8)
$$

where RL is the return loss and $\delta[n]$ is the relative loss of the reflection path to the direct path.

When the locations of the UE and the antenna are fixed, $\Delta\theta_r[n]$ in (7) is caused by the additional traveling distance compared to the direct path. Besides, the Doppler frequency shift can be expressed as the differential of the phase of the traveling wave in (5). In other words, the increment of successive two the phase samples of the traveling wave can be integral of the Doppler frequency variances in the sampling interval, $\frac{1}{f_s}$. We define the phase difference of the two successive samples as $\theta_D[n] = \Delta\theta_r[n] - \Delta\theta_r[n - 1]$, and it follows that

$$
\theta_D[n] = 2\pi \int_{\frac{n-1}{f_s}}^{\frac{n}{f_s}} f_{D,r}(t)\,dt = \frac{2\pi f_{D,r}[n]}{f_s}, \quad (9)
$$

where $f_{D,r}[n]$ is the average Doppler frequency of the reflection path in the time duration $[\frac{n-1}{f_s}, \frac{n}{f_s}]$ and can be expressed as $f_{D,r}[n] = f_s \int_{\frac{n-1}{f_s}}^{\frac{n}{f_s}} f_{D,r}(t)\,dt$. Thus, the Doppler frequency can be obtained by

$$
f_{D,r}[n] = \frac{f_s \theta_D[n]}{2\pi}. \quad (10)
$$

III. MICRO-DOPPLER ESTIMATION

After discussing sounding waveform selection briefly, we now first present synchronization method and our Doppler shift estimation method in this section.

A. Sounding Waveform and Synchronization

The sounding waveform in a system should meet the requirements of delay resolution, frequency resolution, and synchronization. Ambiguity function (AF) succinctly characterizes the behaviors of a waveform is an analytical tool for waveform design and analysis.

The four possible candidates are continuous wave (CW), linear frequency modulation continuous wave (L-FMCW) [13], stepped FMCW (S-FMCW) [13], and frequency-domain Zadoff-Chu sequence (FD-ZC) [14]. Because the L-FMCW has better resolution and detection range for both time and frequency domains, it is used as the sounding waveform in our study.

We apply the correlator, implemented by the match filter with the sounding waveform, to synchronize the received signal by finding the delay, the amplitude gain, and the phase of the received signal. The correlation, $R_{yx}[m]$, can be expressed as

$$
R_{yx}[m] = \sum_{n=0}^{N_x-1} (y[n + m]x^*[n]), \quad (11)
$$

where m is the delay of the direct path and N_x is the length of the sounding waveform. Assume $\{a_d[n], \theta_d[n]\}$ are fixed within N_x samples. We can omit index n from them as $\{a_d, \theta_d\}$, the $R_{yx}[m]$ can be expressed as

$$
\begin{aligned}
R_{yx}[m] = {}& \underbrace{a_d e^{j\theta_d} \sum_{n=0}^{N_x-1} x[n - n_d + m]x^*[n]}_{\text{Desired information}} \\
& + \underbrace{\sum_{n=0}^{N_x-1} \{a_r[n]x[n - n_d + m]x^*[n]e^{j(\theta_d[n+m]+\Delta\theta_r[n+m])}\}}_{\text{Self interference}} \\
& + \underbrace{\sum_{n=0}^{N_x-1} \{w[n + m]x^*[n]\}}_{\text{AWGN}}. \quad (12)
\end{aligned}
$$

Note that when $m = n_d$ in (12), $R_{yx}[n_d]$ is the maximum value over all range of interest. Thus, the delay, the amplitude gain, and the phase of the direct path can be estimated by

$$
\begin{cases}
\hat{n}_d = \arg\max_{m} R_{yx}[m], \\
\{\hat{a}_d, \hat{\theta}_d\} = \{\mathrm{abs}(R_{yx}[\hat{n}_d]), \mathrm{angle}(R_{yx}[\hat{n}_d])\}.
\end{cases} \quad (13)
$$

Although the correlation of the sounding waveform has a processing gain against the AWGN, the signal from the reflection path causes self-interference to estimate the synchronization parameters in (12). If $a_r[n]$ is small enough, the phase and the gain of the synchronization parameters are approaching to the direct path.

B. Estimation

From (7), the reflection path response can be estimated by

$$
\hat{a}_r[n]e^{j\Delta\hat{\theta}_r[n]} = \frac{y[n] - \hat{a}_d x[n - \hat{n}_d]e^{j\hat{\theta}_d}}{x[n - \hat{n}_d]e^{j\hat{\theta}_d}}, \quad (14)
$$

where the parameters corresponding to the direct path in (7) can be estimated and are denoted as $\{\hat{n}_d, \hat{a}_d, \hat{\theta}_d\}$ from (13) by using (12). Based on (10), the Doppler frequency can be estimated by

$$
\hat{f}_{D,r}[n] = \frac{f_s \hat{\theta}_D[n]}{2\pi} = \frac{f_s \,\mathrm{Arg}\left(\frac{\hat{a}_r[n]e^{j\Delta\hat{\theta}_r[n]}}{\hat{a}_r[n-1]e^{j\Delta\hat{\theta}_r[n-1]}}\right)}{2\pi}, \quad (15)
$$

when the power level, $|\hat{a}_r[n]|^2$, is larger than a threshold P_{thd}. In the above, we have used a threshold to make sure that the phase corresponding to high amplitude is used for estimation since that corresponding to low amplitude does not carrier worthy information for accurate estimation. Furthermore, the Doppler frequency estimation accuracy can been improved by averaging $2N_{avg} + 1$ adjacent estimates as the following

$$
\bar{f}_{D,r}[n] = \frac{\sum_{m=-N_{avg}}^{N_{avg}} \hat{f}_{D,r}[n + m]}{2N_{avg} + 1}, \quad (16)
$$

where N_{avg} is chosen to balance the one-shot estimation error and variation of the Doppler frequency.
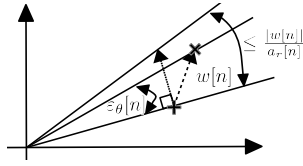
Fig. 3. Relationships for phase error estimation.

C. Bonds of Phase and Frequency Estimation Errors

Fig. 3 demonstrates the relationship of phase estimation and time, where the symbol $\times$ denotes the ideal reflection signal, $a_r[n]e^{j\Delta\theta_r[n]}$, while the symbol $+$ denotes the received signal from the ideal reflection signal by noise, which is expressed as $\hat{a}_r[n]e^{j\Delta\hat{\theta}_r[n]} = a_r[n]e^{j\Delta\theta_r[n]} + w[n]$ as (14), and the phase estimation error is caused by the channel noise. Therefore, the bound of the phase estimation error, $\varepsilon_\theta[n] = \Delta\theta_r[n] - \Delta\hat{\theta}_r[n]$, can be expressed as

$$|\varepsilon_\theta[n]| \leq \tan^{-1}\frac{|w[n]|}{a_r[n]} \leq \frac{|w[n]|}{a_r[n]}. \tag{17}$$

When applying the expectation calculation to $\varepsilon_\theta[n]$, it follows $\mathrm{E}(|\varepsilon_\theta[n]|^2) \leq \mathrm{E}(\frac{|w[n]|^2}{|a_r[n]|^2})$. Since $w[n]$ and $\frac{1}{a_r[n]}$ are independent, the $\mathrm{E}(\frac{|w[n]|^2}{|a_r[n]|^2}) = \mathrm{E}(|w[n]|^2)\mathrm{E}(\frac{1}{|a_r[n]|^2})$. Because L-FMCW is a constant envelope waveform, $\mathrm{E}(|a_r[n]|^2) = |a_r[n]|^2$. With $\mathrm{E}(|a_r[n]|^2) = \frac{\sigma_s^2}{10^{\frac{RL+\delta[n]}{10}}}$ in (8) and $\sigma_w^2 = \mathrm{E}(|w[n]|^2)$, it follows

$$\mathrm{E}(|\varepsilon_\theta[n]|^2) \leq \mathrm{E}\left(\frac{|w[n]|^2}{|a_r[n]|^2}\right) = \frac{\sigma_w^2 10^{\frac{RL+\delta[n]}{10}}}{\sigma_s^2}.$$

The RMS of phase error can be expressed as

$$10\log\mathrm{E}(|\varepsilon_\theta[n]|^2) \leq RL + \delta[n] - 10\log\frac{\sigma_s^2}{\sigma_w^2}, \tag{18}$$

where $10\log\frac{\sigma_s^2}{\sigma_w^2}$ is signal-to-noise ratio (SNR). And $\delta[n]$ can be approximated by

$$\delta[n] = 20\log(d_{UE} + d_1(1 + \sec 2\theta_e)) - 20\log d_{UE}$$
$$\approx \frac{20d_{ant}}{d_{UE}\ln 10}(\cos 2\theta_e + 1) \approx 0, \text{ when } d_{UE} \gg d_{ant}. \tag{19}$$

Since $\hat{f}_{D,r}[n]$ is derived from the two successive phase estimation in (10), the Doppler frequency RMS error $\varepsilon_{f_{D,r}}[n]$ can be expressed as

$$\varepsilon_{f_{D,r}}[n] = \frac{2f_s\Delta\varepsilon_\theta[n]}{2\pi} \Rightarrow \mathrm{E}(|\varepsilon_{f_{D,r}}[n]|^2) \leq \frac{f_s^2\sigma_w^2 10^{\frac{RL+\delta[n]}{10}}}{\pi^2\sigma_s^2},$$

where $\Delta\varepsilon_\theta[n] = \varepsilon_\theta[n] - \varepsilon_\theta[n-1]$. Then, we can have

$$10\log\mathrm{E}(|\varepsilon_{f_{D,r}}[n]|^2) < 20\log(\frac{f_s}{\pi}) + RL - SNR. \tag{20}$$

IV. SIMULATIONS RESULTS

In this section, we first validate the proposed algorithm with the L-FMCW sounding waveform, and then evaluate the effects of carrier frequency, return loss of the propellers, and the sampling frequency of transmission and reception. The

TABLE II
SIMULATION PARAMETERS

Sym.	Description	Value	Unit
f_c	Carrier frequency	**2.5**, 38	GHz
RL	Return loss	**5**, 15	dB
f_s	Sampling frequency	30, **60**, 480	ksps

(a) Phase $\hat{\theta}_D$
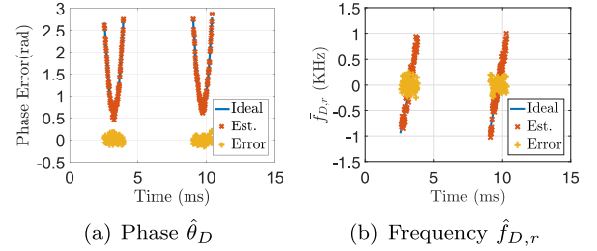
(b) Frequency $\hat{f}_{D,r}$

Fig. 4. $\hat{\theta}_D$ and $\hat{f}_{D,r}$ estimations for algorithm validation.

carrier frequency is ranged from LTE/WiFi service band to the reserved band for millimeter wave (mmWave) communications. The parameters in Table II are adopted in simulation and the default values of other parameters are emphasized as bold. Doppler frequency is estimated by (16) with $N_{avg} = 4$.

A. Algorithm Validation

In Fig. 4(a), the period of the reflection path is determined by $\frac{60}{f_m N_b} \approx 6.494$ msec, with $f_m = 4620$ rpm as the same as that in [8] and $N_b = 2$ as in Table I. Applying $D_p = 254$ mm and $d_{ant} = 200$ mm in Table I to (4), θ_{rz} is $\sin^{-1}\frac{D_p}{4d_{ant}} \approx 0.32$ rad, and the duration of the reflection signal active in the receiver is about 1.323 msec, obtained by $\frac{2\times 0.32\times 6.494}{\pi}$.

Fig. 4(b) shows Doppler frequency $\bar{f}_{D,r}$ obtained from (16). The estimated Doppler frequency $\hat{f}_{D,r}$ increases with samples in time domain in Fig. 4(b). The maximum Doppler frequency can be obtained from (5), where $\theta_e = 0.32$ rad. The approximated Doppler frequency is about 963.09 Hz and matches the results in Fig. 4(b). The maximum error for $\hat{\theta}_D$ and $\hat{f}_{D,r}$ are 0.2 rad and 200 Hz as shown in Fig. 4, respectively. Although the Doppler frequency peak error is as high as 200 Hz, the probability is low and resulting from an example of the poor system parameters.

The estimated periodicity and the maximum frequency of micro-Doppler effect based on the proposed model and detection method are consistent with the results of [8] based on the outdoor measurements. This comparison aims to demonstrate the efficacy of computer simulations.

B. Parameters Evaluation

Fig. 5 shows that the phase ambiguity occurs at low SNR or low value of $\frac{f_c}{f_s}$, where f_c is the carrier frequency and f_s is the sampling frequency. Once the phase ambiguity occurs, the phase estimation will be wrapped in the range of $[-\pi, \pi)$ and then fail to estimate the micro-Doppler frequency correctly. From (20), the RMS of $\varepsilon_{f_{D,r}}[n]$ linearly decreases with the SNR of the channel logarithmically.

The RMS values of $\varepsilon_{f_{D,r}}[n]$, depicted in the circle-line, the cross-line, and the diamond-line curves, depart from the
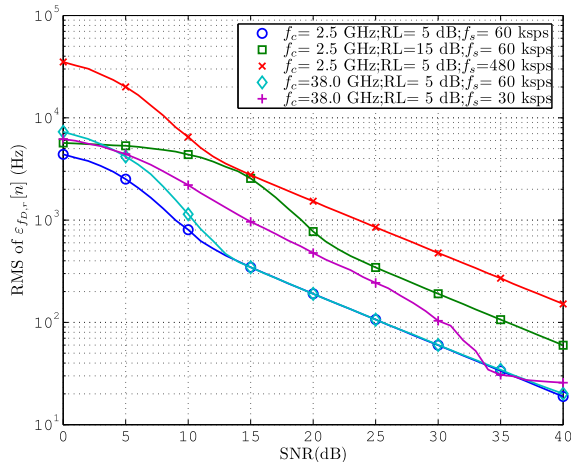
Fig. 5. $f_{D,r}$ RMS error for several cases.

theoretical line when $SNR \leq 15$ dB, which is called critical points. Moreover, the square-line of $RL = 15$ dB, $f_c = 2.5$ GHz, and $f_s = 60$ kilo samples per second (ksps) departs from the theoretical line when $SNR \leq 25$ dB. This is because of the effective SNR of the reflection path of larger RL, e.g., $RL = 15$ dB expressed as the square-line, is smaller than that of the circle-line, $RL = 5$ dB by 10 dB. Thus, the RMS of $\varepsilon_{f_{D,r}}[n]$ for the square-line is shifted 10 dB compared to that for the circle-line. For the same reason, the RMS of $\varepsilon_{f_{D,r}}[n]$ for the square-line is greater than that for the circle-line and saturated when approaching toward the lower SNR.

Now we consider the impact of sampling frequency on the estimate errors by observing the required SNRs for the same RMS of $\varepsilon_{f_{D,r}}[n]$ at different sampling frequencies. For example, the required SNR for the RMS = 200 Hz of the cross-line of $f_s = 60$ ksps is greater than the squared-line of $f_s = 480$ ksps by 18 dB. Lower sampling frequency contributes time average effect on the Doppler estimation so that the RMS of $\varepsilon_{f_{D,r}}[n]$ at the high sampling frequency is smaller than the lower sampling frequency.

The impact of the carrier frequency on the RMS of $\varepsilon_{f_{D,r}}[n]$ is shown in the circle-line and the diamond-line curves, which are the same parameters except for carrier frequency. The effect of carrier frequency on $\varepsilon_{f_{D,r}}[n]$ is not significant when SNR is larger than the critical point. When the SNR is smaller than the critical point, the RMS of $\varepsilon_{f_{D,r}}[n]$ at the low carrier frequency is smaller than that at the high carrier frequency because of phase ambiguity.

Finally, we emphasize the phase ambiguity at high carrier frequency by decreasing the sampling rate of the diamond-line from 60 ksps to 30 ksps. The RMS of $\varepsilon_{f_{D,r}}[n]$ of 30 ksps is plotted as the plus-line and does not follow (20). The deviation of the plus-line is caused when f_s is too slow compared to the phase generated by the Doppler frequency. The estimated phase sampled by a smaller f_s in Doppler frequency estimation is out of the principal value range, so fails to estimate the correct micro-Doppler frequency. This issue can be solved by increasing f_s to 60 ksps, and that makes the estimated phase lie in the principal value range at the expense of the loss of the RMS.

Accordingly, given f_c and a return loss, we can detect and estimate the micro-Doppler frequency correctly by choosing the proper f_s and SNR. Under the well-designed parameters of 60 ksps and 40 dB SNR for 2.5 GHz carrier frequency and 5 dB RL, the averaged estimated RMS error of micro-Doppler is about 18.83 Hz, i.e., 1.95%.

V. CONCLUSION

In this letter, we proposed a method to evaluate the micro-Doppler effect in the air-to-ground channel. We showed the loss of the proposed method with optimized parameters is about 1.93% of the maximum Doppler shift. To our best knowledge, neither the FMCW non-coherent nor the STFT methods can detect the micro-Doppler shift in the sub-6 GHz. We showed the effects of the parameters on detecting micro-Doppler and how to improve the estimation accuracy. In the future, we would plan to validate our method by the experiments inside an anechoic chamber or in a real flying field and how the micro-Doppler affects the network traffic behaviors.

REFERENCES

[1] *UAV Utilization of Cellular Services—Enabling Safe and Scalable Operation*, Standard ATIS-I-0000060, Sep. 2017.

[2] W. Khawaja, I. Guvenc, D. W. Matolak, U.-C. Fiebig, and N. Schneckenburger, "A survey of air-to-ground propagation channel modeling for unmanned aerial vehicles," *IEEE Commun. Surveys Tuts.*, vol. 21, no. 3, pp. 2361–2391, 3rd Quart., 2019.

[3] A. A. Khuwaja, Y. Chen, N. Zhao, M.-S. Alouini, and P. Dobbins, "A survey of channel modeling for UAV communications," *IEEE Commun. Surveys Tuts.*, vol. 20, no. 4, pp. 2804–2821, 4th Quart., 2018.

[4] D. W. Matolak and R. Sun, "Air–ground channel characterization for unmanned aircraft systems—Part III: The suburban and near-urban environments," *IEEE Trans. Veh. Technol.*, vol. 66, no. 8, pp. 6607–6618, Aug. 2017.

[5] R. M. Gutierrez, H. Yu, Y. Rong, and D. W. Bliss, "Time and frequency dispersion characteristics of the UAS wireless channel in residential and mountainous desert terrains," in *Proc. 14th IEEE Annu. Consum. Commun. Netw. Conf. (CCNC)*, Las Vegas, NV, USA, 2017, pp. 516–521.

[6] V. C. Chen, *The Micro-Doppler Effect in Radar*. Norwood, MA, USA; Artech House, 2011.

[7] J. J. M. de Wit, R. I. A. Harmanny, and G. Prémel-Cabic, "Micro-Doppler analysis of small UAVs," in *Proc. IEEE 9th Eur. Radar Conf.*, Amsterdam, The Netherlands, 2012, pp. 210–213.

[8] J. J. M. de Wit, R. I. A. Harmanny, and P. Molchanov, "Radar micro-Doppler feature extraction using the singular value decomposition," in *Proc. Int. Radar Conf.*, Lille, France, 2014, pp. 1–6.

[9] R. I. A. Harmanny, J. J. M. de Wit, and G. P. Cabic, "Radar micro-Doppler feature extraction using the spectrogram and the cepstrogram," in *Proc. 11th Eur. Radar Conf.*, Rome, Italy, 2014, pp. 165–168.

[10] H.-A. Hou and L.-C. Wang, "Analysis on time-variant air-to-ground radio communication channel for rotary-wing UAVs," in *Proc. IEEE 89th Veh. Technol. Conf. (VTC-Spring)*, Kuala Lumpur, Malaysia, 2019, pp. 1–6.

[11] Z. Zhang, L. Li, X. Liu, W. Liang, and Z. Han, "Matching-based resource allocation and distributed power control using mean field game in the NOMA-based UAV networks," in *Proc. Asia–Pac. Signal Inf. Process. Assoc. Annu. Summit Conf. (APSIPA ASC)*, Honolulu, HI, USA, 2018, pp. 420–426.

[12] Y. Liu, Z. Qin, Y. Cai, Y. Gao, G. Y. Li, and A. Nallanathan, "UAV communications based on non-orthogonal multiple access," *IEEE Wireless Commun. Mag.*, vol. 26, no. 1, pp. 52–57, Feb. 2019.

[13] M. Richards, *Fundamentals of Radar Signal Processing*. New York, NY, USA: McGraw Hill, 2005.

[14] *3GPP; Technical Specification Group Radio Access Network; New Radio (NR); Physical Channels and Modulation (Release 15), Rev. 15.0.0*, 3GPP Standard TS 38.211, Dec. 2017.